Acta Neurochir (2015) 157:689–698
DOI 10.1007/s00701-014-2339-7

EXPERIMENTAL RESEARCH - PEDIATRICS

Changes of fractional anisotropy (FA) and apparent diffusion coefficient (ADC) in the model of experimental acute hydrocephalus in rabbits

Maxim A. Shevtsov · Konstantin A. Senkevich · Alexander V. Kim · Kseniia A. Gerasimova · Tatyana N. Trofimova · Galina V. Kataeva · Sviatoslav V. Medvedev · Olga I. Smirnova · Zhanna I. Savintseva · Marina G. Martynova · Olga A. Bystrova · Emil Pitkin · Galina Y. Yukina · William A. Khachatryan

Received: 21 October 2014 / Accepted: 27 December 2014 / Published online: 16 January 2015

Abstract
Background To study the integrity of white matter, we investigated the correlation between the changes in neuroradiological and morphological parameters in an animal model of acute obstructive hydrocephalus.
Methods Hydrocephalus was induced in New Zealand rabbits ($n=10$) by stereotactic injection of kaolin into the lateral ventricles. Control animals received saline in place of kaolin ($n=10$). The progression of hydrocephalus was assessed using magnetic resonance imaging. Regional fractional anisotropy (FA) and the apparent diffusion coefficient (ADC) were measured in several white matter regions before and after the infusion of kaolin. Morphology of myelinated nerve fibers as well as of the blood–brain barrier were studied with the help of transmission electron microscopy (TEM) and light microscopy.
Results Compared with control animals, kaolin injection into the ventricles resulted in a dramatic increase in ventricular volume with compression of basal cisterns, brain shift and periventricular edema (as observed on magnetic resonance imaging [MRI]). The values of ADC in the periventricular and periaqueductal areas significantly increased in the experimental group ($P<0.05$). FA decreased by a factor of 2 in the zones of periventricular, periaqueductal white matter and corpus collosum. Histological analysis demonstrated the impairment of the white matter and necrobiotic changes in the cortex. Microsctructural alterations of the myelin fibers were further proved with the help of TEM. Blood–brain barrier ultrastructure assessment showed the loss of its integrity.
Conclusions The study demonstrated the correlation of the neuroradiological parameters with morphological changes. The abnormality of the FA and ADC parameters in the obstructive hydrocephalus represents a significant implication for the diagnostics and management of hydrocephalus in patients.

M. A. Shevtsov · A. V. Kim · K. A. Gerasimova · W. A. Khachatryan
A.L. Polenov Russian Scientific Research Institute of Neurosurgery, 191014Mayakovsky str. 12, St. Petersburg, Russia

K. A. Senkevich · G. Y. Yukina
I.P. Pavlov State Medical University, 197022L. Tolstoi str. 6-8, St. Petersburg, Russia

M. A. Shevtsov (✉) · M. G. Martynova · O. A. Bystrova
Institute of Cytology of the Russian Academy of Sciences (RAS), 194064Tikhoretsky Ave. 4, St. Petersburg, Russia
e-mail: shevtsov-max@mail.ru

T. N. Trofimova · G. V. Kataeva · S. V. Medvedev · O. I. Smirnova · Z. I. Savintseva
N.P. Bechtereva Institute of the Human Brain of the Russian Academy of Sciences (RAS), 197376Akademika Pavlova str. 9, St. Petersburg, Russia

E. Pitkin
The Wharton School, University of Pennsylvania, 3730 Walnut St., Philadelphia, PA 19104, USA

Keywords Hydrocephalus · Magnetic resonance imaging · Fractional anisotropy · Apparent diffusion coefficient · White matter · Ventriculomegaly

Introduction

Hydrocephalus represents a common and complex pathology caused by physical or functional obstruction of the cerebrospinal fluid (CSF) flow with an incidence rate of 1.1 in 1,000 infants [40]. Clinically hydrocephalus presents as progressive ventricular dilatation and is typically divided into noncommunicating and communicating subtypes [17]. Noncommunicating hydrocephalus results from the obstruction of the CSF pathways (e.g., tumor, arteriovenous malformation [AVM], etc.). Communicating hydrocephalus mostly occurs following subarachnoid hemorrhage and results from the impaired absorption of CSF at the level of the arachnoid granulations [8]. The predominant mode of hydrocephalus treatment constitutes a ventriculoperitoneal (VP) shunting, though other alternative surgical approaches (e.g., endoscopic ventriculostomy) exist [28, 29, 35, 36].

Several recent models of obstructive hydrocephalus were proposed in various animal species including mice, rats, cats, dogs, and sheep [1, 10, 11, 22–24, 37, 42]. In these models the authors mostly focused on the parameter of the ventricular size for characterization of the hydrocephalus and subsequent surgical treatment. At the same time, other characteristics including neuroradiological parameters are of high importance in the diagnosis and assessment of treatment efficacy of hydrocephalus. Thus, in a recent study of Eskandari et al. [16] in the model of kaolin-induced hydrocephalus in cats, it was shown that fraction anisotropy (FA) significantly decreased in the acute stage (<6 weeks) of hydrocephalus and could be reversed in early stages of reservoir placement. However the correlation between the observed radiological changes and corresponding morphological alterations was less studied. Thus, in the work by Chua et al. [9] it was shown that a change in the apparent diffusion coefficient (ADC) and FA parameters did not result in differences in axonal and myelin morphology in the white matter regions. Though the authors could induce severe ventriculomegaly with neuro-behavioral changes in premature rabbit pups by intraperitoneal injection of glycerol, they observed only slight changes in the myelin ultrastructure (e.g., intra-axonal vacuoles, autophagosomes).

In the current study, we aimed to assess the morphological as well as corresponding neuro-radiological changes of the white matter in the model of acute hydrocephalus in rabbits. We used the diffusion tensor imaging (DTI) technique for characterization in vivo the anisotropic diffusion in white matter and subsequently compared the evaluated parameters with the electron and light microscopy data.

Materials and methods

Model of acute obstructive hydrocephalus

Animals

Male New Zealand rabbits weighing 4.5–5.5 kg were purchased from an animal nursery ("Rappolovo" Russian Academy of Medical Sciences [RAMN], St. Petersburg, Russia). Animals were housed in cages under controlled temperature (22±1 °C) and humidity (55±5 °C), and a 12-h light–dark cycle, with food and water ad libitum. All animal experiments were approved by the local ethical committee of I.P. Pavlov State Medical University (St. Petersburg, Russia).

Anesthesia and craniotomy

The animals were intravenously anesthetized with 1 ml ketamine (Calypsol; Gedeon Richter, Budapest, Hungary) and 0.75 ml xylazine (Rometar; Bioveta, Ivanovice na Hané, Czech Republic), and placed in a stereotactic head frame. Continuous anesthesia was provided by intravenous administration of droperidol, ketamine and xylazine over 2 h. During surgery, heart rate (at 130–325 beats/min) and respiratory rate (at 32–60 per min) were monitored, as well as blood pressure (at 90–130/90–60 mm Hg) and body temperature (at level 38.5–39.6 °C). The head was shaved and the scalp was incised longitudinally (4 cm). A burr hole was placed 5 mm to the sagittal suture and 1 mm posterior to coronal suture. Following this, the craniotomy was performed.

Ultrasound examination

For sonography, an ultrasound system (MyLab; Esaote, Genova, Italy) with a 3– to 13-MHz linear probe was utilized. After bone flap removal, the standard B-mode imaging was acquired. All lesions were initially evaluated with B-mode imaging: they were defined as highly hyperechoic, mildly hyperechoic, isoechoic, and hypoechoic compared with normal brain parenchyma. Other lesion characteristics taken into account were diffuse or circumscribed appearance, and homogeneous versus heterogeneous lesions. The volumetrics were performed on the two identified axes and calculated.

Injection of kaolin

Following craniotomy, the ultrasound sensor in standard B-mode was placed over the dura mater. The coordinates for the

infusion of the kaolin into the lateral ventricle were calculated. Hydrocephaly was induced by injection of 0.4 ml of 30 % kaolin solution (Acros Organics; Sigma, St. Louis, MO, USA). Injection of 0.01 M phosphate-buffer solution (PBS) was used as the control. For injection a 22-gauge needle was applied. No CSF leakage was observed at the entry site of the injection. A total of 20 rabbits were used for the study as follows: (1) control group (n=10); (2) experimental group (n=10).

Magnetic resonance imaging

Magnetic resonance imaging (MRI) scans were performed on a 3.0-T whole-body scanner (Achieva; Philips Medical Systems, Best, The Netherlands) using an eight-channel head coil. The rabbit position in the head coil was supine; we then used the positioning lasers to send the spot between the rabbit's eyes to the magnet isocenter. To obtain the axial T2-weighted images through the entire brain, we used a TSE (turbo spin-echo) sequence with time for repetition/time for echo (TR/TE) of 4,800/90 ms, slice-thickness of 3 mm, a slice gap of 0, turbo factor of 11, 124×86×87-mm field of view, a voxel size of 0.38×0.535, a 400 reconstruction matrix, an NSA of 2. To obtain the sagittal T2 3D-weighted images through the entire brain we used a TSE (turbo spin-echo) sequence with a TR/TE of 2500/309 ms, turbo factor of 100, 250×250×180-mm field of view, a voxel size of 1.0×1.0×0.5, a 512 reconstruction matrix, an NSA of 2. To obtain the sagittal T1 3D-weighted images through the entire brain we used a FFE (fast field echo) sequence with a TR/TE of 500/50 ms, turbo factor of 205, 262×207×160-mm field of view, a voxel size of 0.9×0.9×1.0, a 480 reconstruction matrix, an NSA of 1. To obtain the coronal FLAIR-weighted images through the entire brain we used a IR (inversion-recovery) sequence with a TR/TE of 12,000/140 ms, a IR of 2,850, slice-thickness of 1.5 mm, a slice gap of 0.5, turbo factor of 36, 160×109×77-mm field of view, a voxel size of 0.9×1.0, a 512 reconstruction matrix, an NSA of 1.

To obtain the axial DTI-weighted images through the entire brain we used a SE (spin-echo) sequence with a TR/TE of 1,000/61 ms, slice-thickness of 2 mm, a slice gap of 0, max b factor of 800, 224×224×120-mm field of view, a voxel size of 2.0×2.0, a 128 reconstruction matrix, an NSA of 2. The acquisition time for each rabbit at any stage was 2 min and 50 s for the T2-weighted images, 7 min and 32 s for the T2 3D-weighted images, 8 min and 28 s for the T1 3D-weighted images, 3 min and 12 s for the FLAIR-weighted images, 3 min and 55 s for the DTI-weighted images. The program, Extended MR workspace 2.6.3.4, was used for image processing. Additionally in the regions of interest (ROI) (i.e., periventricular area, cortex, periaqueductal area, corpus callosum) the fractional anisotropy (FA) values were calculated. DWI was acquired using a fast spin echo multislice (TR/TE 3,500/36 ms, field of view 3.6 cm, b values of 0 and 1,000s /mm^2, and 8 averages) in axial directions. Diffusion-weighted imaging (DWI) and ADC maps were separately calculated with diffusion weighting in three orthogonal directions, averaged over directions (mean ADC). DWI and ADC maps were visually assessed for abnormal signal intensity, consistent with restricted diffusion and therefore probable tissue edema. ADC values for ROI measurements were obtained independently by two observers. ROIs included periventricular area, cortex, and periaqueductal area. Measurements were made for both the right and left sides of the brain.

Histological analyses

Four weeks after the operation, the animals' brains were extracted, fixed in 10 % formalin solution and embedded into paraffin. Histological sections were obtained and stained with hematoxylin-eosin (H&E) or by Kluver-Barrera's method.

Transmission electron microscopy

For TEM several samples were obtained from each rabbit from experimental and control groups. The biopsies (2–5 mm) were taken from the periventricluar area, periaqueductal and corpus collosum, and immediately fixed in 4 % glutaraldehyde-cacodylate buffer, pH 7.4 at 4 °C. After 72 h, samples were immersed for secondary fixation in 1 % osmium tetroxide (OsO_4)-0.1 M phosphate buffer (pH 7.4) for 1 h, then dehydrated, embedded in Epon and Araldit, and sectioned with a diamond knife on a LKB ultratome. Ultrathin sections were collected on fine mesh copper or nickel grids, and stained with uranyl acetate and lead citrate for examination with Zeiss Libra 120 electron microscope operated at 80 kV

Statistical analysis

Student's t-test was used to evaluate the differences between control and experimental groups using Statistica Version 5.0 for Windows. P values less than 0.05 were considered statistically significant.

Results

Kaolin injection into the lateral ventricles results in obstructive hydrocephalus

A craniotomy was performed in male rabbits weighing 4.5–5.5 kg to expose the supratentorial brain, leaving the dura mater intact (n=10) (Fig. 1). Registration and targeting of the kaolin injection was done using sonication. Sonications

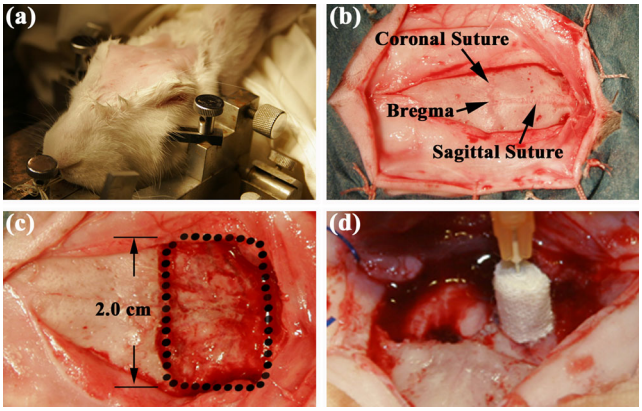

Fig. 1 Intraoperative photos of the experimental hydrocephalus. **a** Fixation of the rabbits head in the head stereotactic frame. **b** Landmarks for craniotomy. **c** Craniotomy performed 1 mm posterior to bregma. **d** Injection of the kaolin into the lateral ventricles

were performed at both 650 kHz and 230 kHz at a range of intensities. The stereotactic coordinates for the kaolin injection were as follows: 5 mm lateral to the sagittal sinus, 5 mm posterior to the bregma, and 5.5–6.5 mm below the dura mater. Additional assessment of the cerebral blood flow (CFM-regimen) before kaolin infusion helped to avoid the damage of the sagittal sinus collaterals. Intraoperative analysis of the lateral ventricular volume was performed using an ultrasound system (MyLab 30; Esaote, Genova, Italy). Thus, the maximum ventricular width was nearly 1.0 mm (Fig. 2a). Following injection of the kaolin, the kaolin on standard ultrasound B-mode appeared hyperechoic compared with brain parenchyma, with a heterogeneous appearance composed of areas with diffuse margins. Size ranged from 1 to 3 mm of maximal

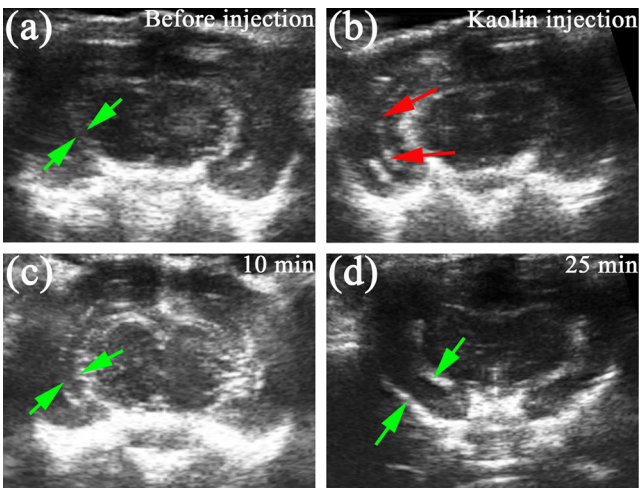

Fig. 2 Intraoperative sonography of the animals brain. **a** Ultrasound scan before the kaolin infusion. **b** Sonography scan obtained immediately after injection of the kaolin. The presence of the kaolin in the ventricle is pointed by *red arrows*. **c** Ten minutes following infusion of kaolin. The size of the ventricle is marked by *green arrows*. **d** Twenty-five minutes following kaolin infusion. The enlargement of the ventricles is demonstrated (*green arrows*)

diameter (Fig. 2b). After 10 min, the kaolin was not observed in the ventricles though minor quantities presented in the lower ventricular horns (Fig. 2c). Quantification of lateral ventricular size showed an increase in ventricular width. Subsequent ultrasound assessment 25 min following kaolin infusion clearly demonstrated a threefold enlargement of the ventricles, equaling 3.5 mm (Fig. 2d). Following injection of the kaolin the bone was placed on the cranium and fixed with biological glue. All animals tolerated the inoculation of kaolin well and quickly recovered after the operation. On the 5th day after the operation we observed ventral and/or lateral strabismus in three out of ten animals, which can be associated with pressure on the mesencephalic tegmentum [10]. On the 2nd week, as a result of the involvement of supratentorial and brainstem structures, we observed alterations in awareness and consciousness, circling, paresis. In two out of ten rabbits we observed the ipsilateral (on the side of kaolin injection) postural reaction deficits that further progressed into the ipsilateral paresis. In eight of ten on the 3rd week the paraparesis developed. In few rabbits we observed head tilt, ataxia, and nystagmus. Nystagmus was horizontal, rotary or vertical and in one of ten animal changed direction with different positions of the head. As a result of the obstructive hydrocephalus on the 4th week all animals developed coma and died.

Hydrocephalus progression causes a change in ADC and FA

The MRI studies for the kaolin-injected animals were performed on the 2nd and 4th weeks after operation. Subsequent MR scans confirmed the development of the obstructive hydrocephalus in all animals (Fig. 3a). Dilatated ventricles compressed the basal cisterns and in several animals resulted in Sylvian aqueductal stenosis. Ventricular deformities also caused a brain shift up to 3 mm. Brain stem deformity was present in four of ten rabbits. After 2 weeks we observed an enlargement of ventricle volume in comparison to control group (Fig. 3b, Table 1). The mean volume was 168.3 ± 15.05 mm^3 and 267.2 ± 27.86 mm^3 for control and kaolin-treated groups, respectively. Four weeks after infusion, we observed further increase in the ventricular volume: 392.4 ± 49.1 mm^3 ($P<0.05$). On the T2-weighted images we observed a periventricular edema that was hyperintensive, as opposed to the low T2 signal from white matter tracts. ADC values were calculated for each of the ROIs for all experimental animals (Fig. 4, Table 2). At the second week after injection of the kaolin, the ADC values were slightly different in the cortex region if compared with control non-treated animals, equaling $143 \pm 21.51 \times 10^{-5}$ mm^2/s and $131 \pm 14.88 \times 10^{-5}$ mm^2/s, respectively ($P<0.05$). Significant differences occurred in the periventricular and periaqueductal ROIs between the control and experimental group following 4 weeks after kaolin infusion. The

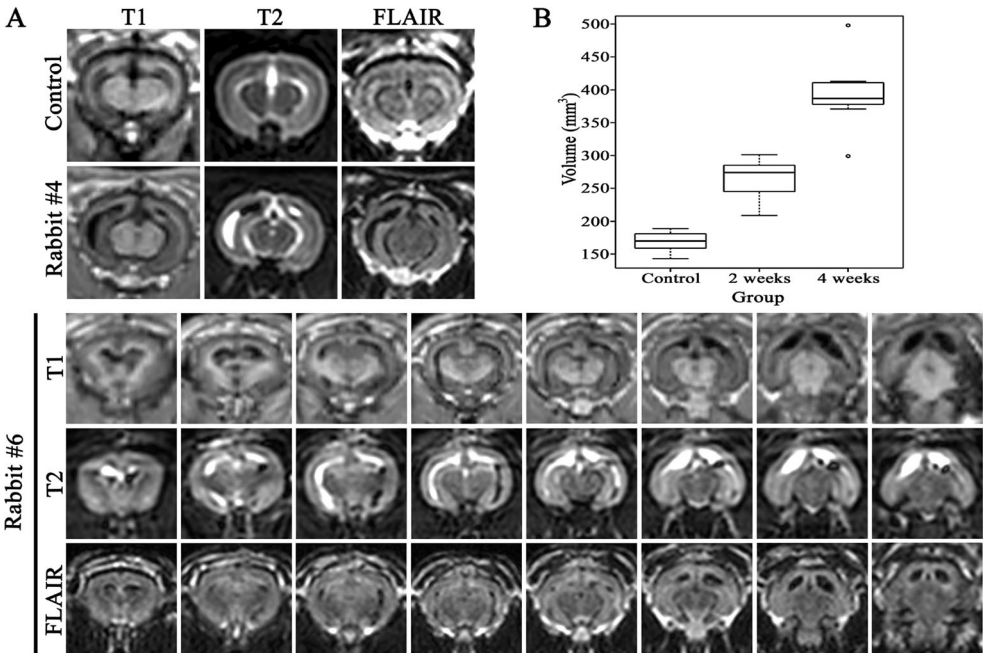

Fig. 3 MRI of the control and experimental rabbits 4 and 6. **a** The MR T1- and T2-weighted, as well as FLAIR MR scans are presented. **b** Boxplots of ventricle volume (mm^3) for control and experimental animals

ADC value was statistically significantly higher than in the control and was $323.9 \pm 39.97 \times 10^{-5}$ mm^2/s (periaqueductal area), $362.6 \pm 41.37 \times 10^{-5}$ mm^2/s (periventricular area) ($P<0.05$). Both ventricular volumes and periventricular, periaqueductal ADCs were significantly correlated ($P<0.001$).

Additionally we calculated anisotropy by using the orientation-independent FA from the DTI maps with the three vector elements. Vector maps were assigned to red (x element, left–right), green (y, anteroposterior), and blue (z, superior–inferior) with proportional intensity scale according to the FA (Fig. 5). Thus, on the tractography images obtained we demonstrated a significant loss of white matter tracts in the experimental hydrocephalic animals 4 weeks following kaolin injection (Fig. 5a). Quantitative analysis was performed using the ROI method settled on the central part of all identifiable white matter fibers, including periventricular tracts, corpus callosum, periaqueductal tracts and cortex (Fig. 5b). In all animals we observed a significant mean FA reduction in evaluated ROIs except cortical tracts in comparison with the ipsilateral regions of healthy controls (Table 3) ($P<0.001$).

Table 1 Mean and standard deviation of ventricle volume (mm^3) for the control, and after 2 and after 4 weeks following injection of kaolin

	Group		
	Control	2 Weeks	4 Weeks
Mean	168.3	267.2	392.4
SD	15.05	27.86	49.1

Development of hydrocephalus leads to dramatic damage of white matter tracts

For the analysis of the impact of hydrocephalus on the rabbits' brains we performed a histological examination (staining with H&E and Kluver-Barrera method) of the brain sections of the control and kaolin-treated animals (Fig. 6a, b). Macroscopic sections revealed an extensive ventricular dilatation. Thus we observed the presence of the kaolin in the choroidal plexus of the ventricles (Fig. 6c, d). Kaolin presented as eosinophilic granules

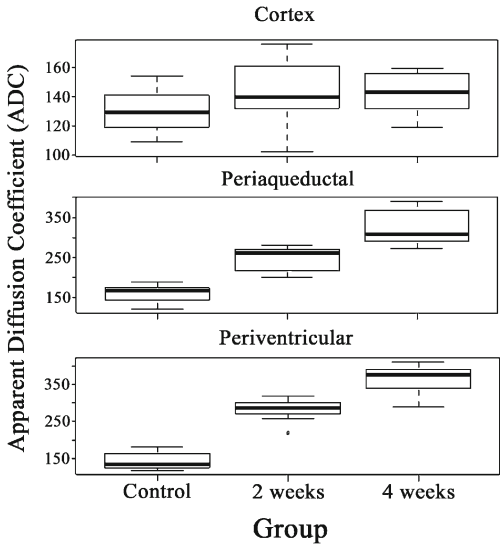

Fig. 4 Boxplots of apparent diffusion coefficients (ADCs). ADC values were obtained for the animals from control and experimental groups in the periventricular, periaqueductal and cortical regions

Table 2 Mean and SD of the apparent diffusion coefficient (ADC) for the control, and after 2 and after 4 weeks following injection of kaolin

		Group		
		Control	2 Weeks	4 Weeks
Cortex	Mean	131	143	142
	SD	14.88	21.51	13.57
Periaqueductal	Mean	162.4	248.4	323.9
	SD	21.37	30.28	39.97
Periventricular	Mean	144.8	283.2	362.6
	SD	21.96	29.27	41.37

Table 3 Mean and standard deviation for fractional anisotropy (FA) for different groups for the cortex, corpus collosum, periaqueductal, and periventricular regions

		Group		
		Control	2 Weeks	4 Weeks
Cortex	Mean	0.361	0.357	0.354
	SD	0.017	0.025	0.017
Corpus collosum	Mean	0.391	0.31	0.21
	SD	0.026	0.03	0.03
Periaqueductal	Mean	0.392	0.289	0.2
	SD	0.026	0.051	0.028
Periventricular	Mean	0.482	0.357	0.217
	SD	0.038	0.035	0.032

on the H&E sections. In a few animals we demonstrated the penetration of the kaolin granules into the brain parenchyma. At the same time we did not observe any inflammatory changes (i.e., infiltration of macrophages, leukocytes) in the site of the kaolin presence (Fig. 6e, f). Further microscopic examination revealed dramatic pericellular edema (Fig. 6g). Moreover we showed perviscular edema that presented throughout the brain tissues (Fig. 6h). Perivascular spaces were significantly enlarged in the periventricular white matter and in the periaqueductal gray matter. Intriguingly, we revealed a noticeable stretching and flattening of the ependymal cells compared with the control animals (Fig. 6i, j). The flattening of the ependymal cells was observed around all ventricles though no apparent proliferation of these cells was revealed. The Kluver-Barrera method for myelin and nerve cells clearly demonstrated extensive necrobiotic changes that were found in the cerebral cortex of the kaolin-treated rabbits (Fig. 6k, l, m, n). In the deep cortex that was close to the white matter, we found pyknotic or dead neurons. Pyramidal cells appeared damaged with

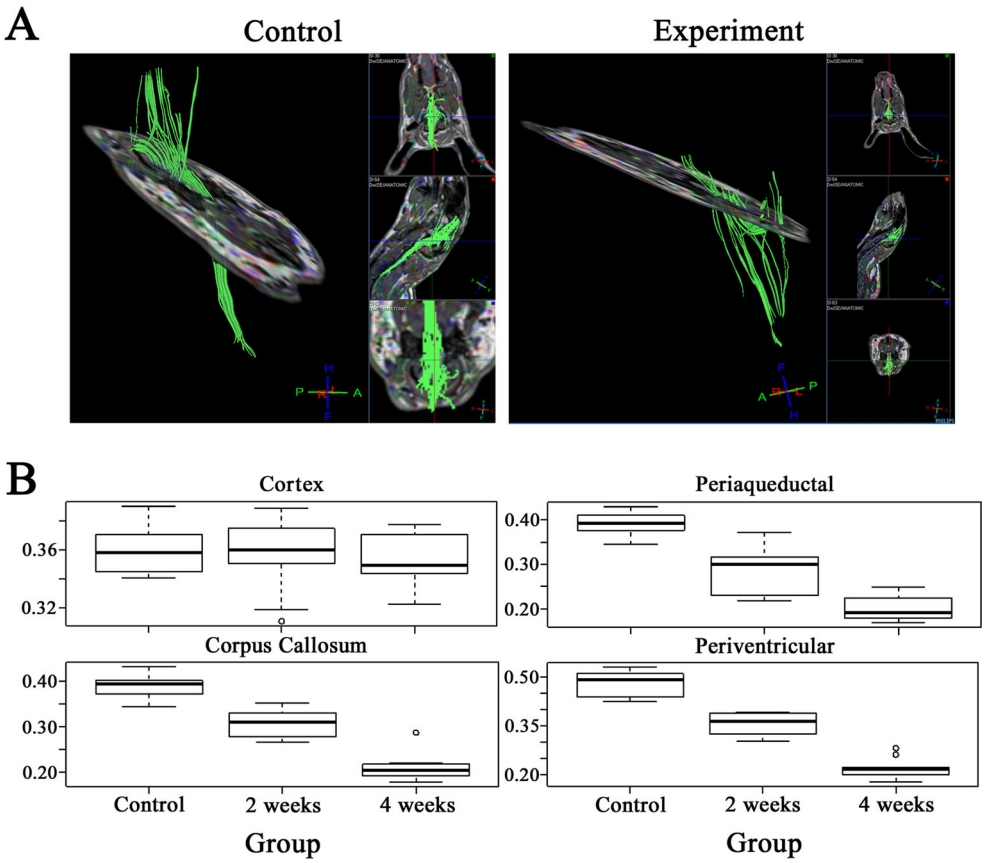

Fig. 5 MR tractography and fractional anisotropy (FA) values of the control and experimental animals. **a** Tractography images for the control and hydrocephalic rabbits. **b** Mean FA with standard deviation is presented as *boxplots*. Regions of interest (ROIs) were assigned to perivetricular, periaqueductal, collosal areas and cortex

numerous vacuoles. In the cortex, we found cells without processes and with a nucleus containing clumped chromatin and condensed nucleolar material. Obstructive hydrocephalus also impaired the architecture of the white matter tracts (Fig. 6o, p). These changes were mostly observed in the periventricular tracts developing syringomyelic cavities (Fig. 6p). These spongy areas were interspersed with areas of less damaged tracts. Microstructural alterations of the white matter were further proved with the help of electron microscopy (Fig. 7). Thus in control brain sections we observed the characteristic lamellae of myelin. Subsequent transmission electron microscopy analysis of kaolin-treated animals demonstrated that myelin sheaths were dramatically distorted and sometimes disrupted (Fig. 7c, d). Also in some samples we did not observe the myelin lamellae. Blood–brain barrier ultrastructure analysis demonstrated the impairment of integrity of the latter with significant change in the morphology. We showed an increasing number of the endothelial cells abluminal vesicles. Moreover, we found the significantly thinned basal lamina of the arterioles especially in the periventricular zones (Fig. 7a, b). Some brain capillaries demonstrated glio-basal dissociation when there was a loss of astrocytic end-feet contact with perivascular layer (Fig. 7f). We also observed a disrupted perivascular neuropil. On precise analysis of endotheliocytes we found that the mitochondria were swollen and smaller in comparison to the control animals (Fig. 7 e).

Discussion

MRI enables noninvasive monitoring of hydrocephalus development. At the same time a certain discrepancy between the observed radiological data and morphological brain changes exists and was addressed in the current study. For analysis of the neuroradiological changes in the hydrocephalus progress we applied a well-established kaolin-induced model in rabbits with minor modifications [15, 18, 25, 30, 39]. As distinct from the previous studies, we performed a craniotomy and injected kaolin into the lateral ventricles under the intraoperative

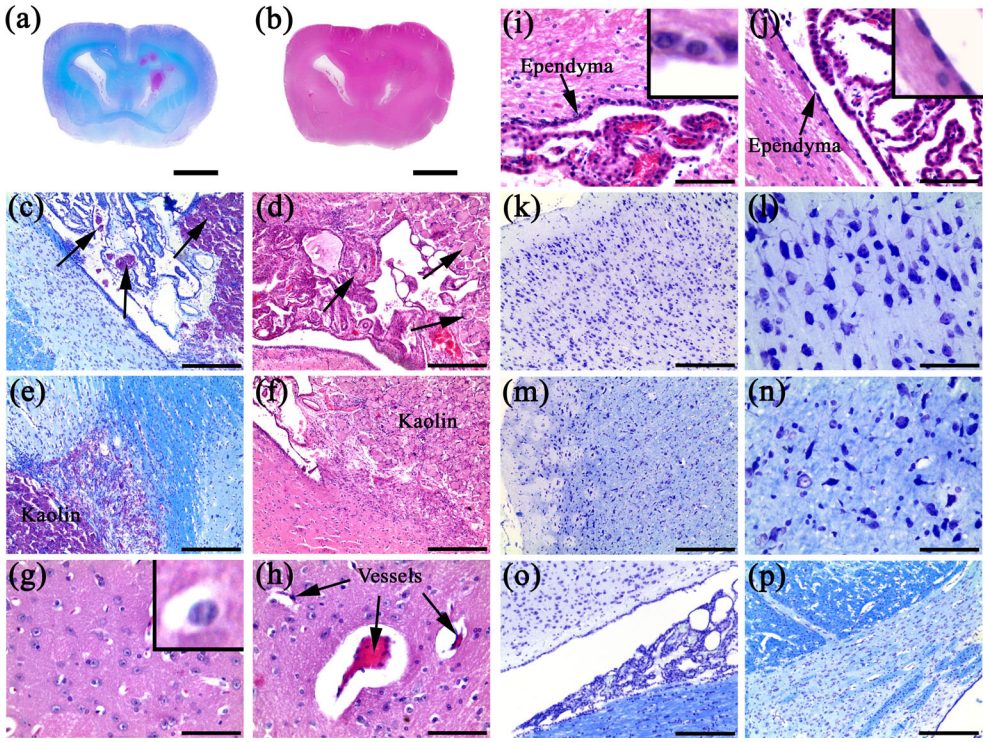

Fig. 6 Histological examination of the hydrocephalic animals. **a**, **b** Macroscopic brain sections stained by the H&E and Kluver-Barrera methods. *Scale bar* 1 cm. **c**, **d** Kaolin presence in the choroidal plexus of the ventricules is indicated by *black solid arrows*. The brain sections were stained by the H&E and Kluver-Barrera methods are shown. *Scale bar* 200 μm. **e**, **f** Penetration of the kaolin into the normal brain tissues. *Scale bar* 200 μm. **g** Pericellular edema in the H&E brain sections. Scale bar, 75 μm. **f** Perivascular edema in the H&E stained sections. *Scale bar* 75 μm. **i** Ependymal cells in control and **j** experimental animal. The stretching of the ependymal cells is shown. *Scale bar* 75 μm. **k**, **i** Cortex of the control rabbit stained by the Kluver-Barrera method. *Scale bar* for **k** is 200 μm, and for **j** is 75 μm. **m**, **n** Cortex of the hydrocephalic rabbit stained by the Kluver-Barrera method. The necrobiotic changes of the neurons are demonstrated. *Scale bar* for **m** is 200 μm, and for **n** is 75 μm. **o** Periventricular white matter for the control animal stained by the Kluver-Barrera method. *Scale bar* 200 μm. **p** Periventricular white matter for the experimental animal stained by the Kluver-Barrera method. Numerous disruptions in the white matter are demonstrated. *Scale bar* 200 μm

ultrasonographic control (Fig. 2). This method provided reliable stereotactic coordinates for kaolin infusion and immediate control for the induction of the hydrocephalus. Thereby, 25 min after injection we already observed a threefold increase in the ventricular volume (Fig. 2d).

Acute obstructive hydrocephalus clinically resulted in the ventriculomegaly with dramatic neuro-behavioral changes (Fig. 3). Moreover, the rapid enlargement of the ventricles caused the impairment of the white matter in the periventricular zones and corpus callosum, resulting in the decrease of FA values compared with control animals (Fig. 5). Precise TEM analysis of the ultrastructure of the myelinated fibers revealed damage to the tracts (Fig. 7). The demyelinization process could be found in the hydrocephalus and was reported to be reversible in an experimental model [12]. As was shown by Yuan et al. [45], FA could be abnormal in multiple regions of white matter in the model of infantile hydrocephalus in rats. Previously, a vascular mechanism underlying the observed changes was proposed [32, 46]. Thus, cerebral blood flow (CBF) values (according to MRI, CT, SPECT data) are significantly reduced causing hypoxic and oxidative damage of the white matter fibers [13, 14, 20, 27, 32, 46]. In a recent study by Del Bigio et al. [13], it was demonstrated that hypoxia via peroxidation and nitrosylation caused significant brain damage in young rodents with hydrocephalus. Hypoperfusion of the white matter may also cause the cytotoxic edema secondary to impaired cell energy metabolism that is detected by the increased lactate levels according to MR spectroscopy data [3, 34]. Neuronal damage that was detected in the cortex according to Kluver-Barrera staining method (Fig. 6 k, l, m, n) could also be attributed to the metabolic and biochemical disturbances [26, 38]. Thus, Braun et al. [2, 4, 5] with the help of 1H MRS, revealed the decreased ratios of N-acetyl aspartate/choline (NAA/Cho) and creatine/choline (tCr/Cho) indicating the neuronal loss/dysfunction or changes in membrane phospholipid metabolism. Among other microscopic morphological changes, we observed the stretching of ependymal cells (Fig. 6 i, j), which agrees with data by Weller et al. [43].

Moreover, we observed that the ADC values in white matter were increased because of accumulation of free extracellular water and the development of periventricular edema (Fig. 4). Elevation of the ADC values could be attributed to the integrity loss of the blood–brain barrier. Thus, TEM clearly demonstrated the ultrastructure impairment of the blood–brain barrier in the hydrocephalic rabbits (Fig. 7). Observed microscopic changes are in accord with previously published observations of ultrastuctural changes in blood–brain barrier in patients with congenital hydrocephalus [6]. Moreover, revealed swollen mitochondria in the endothelial cells indicate the cellular dysfunction due to oxidative stress [33, 44]. Recently, Del Bigio et al. [14] quantitatively measured the blood–brain barrier permeability changes on T1-weighted images following injection of gadolinium diethylenetriamine penta-acetate (Gd-DTPA) tracer in hydrocephalus, proving the integrity loss of the blood–brain barrier. We also observed the thinning of the basal membrane in all brain samples of the experimental group (Fig. 7). Thus, Ueno et al. [41] demonstrated that decrease in thickness of the basal lamina is paralleled with increased vascular permeability.

The results obtained provide a rationale for the application of FA and ADC parameters in clinical practice. In a recent

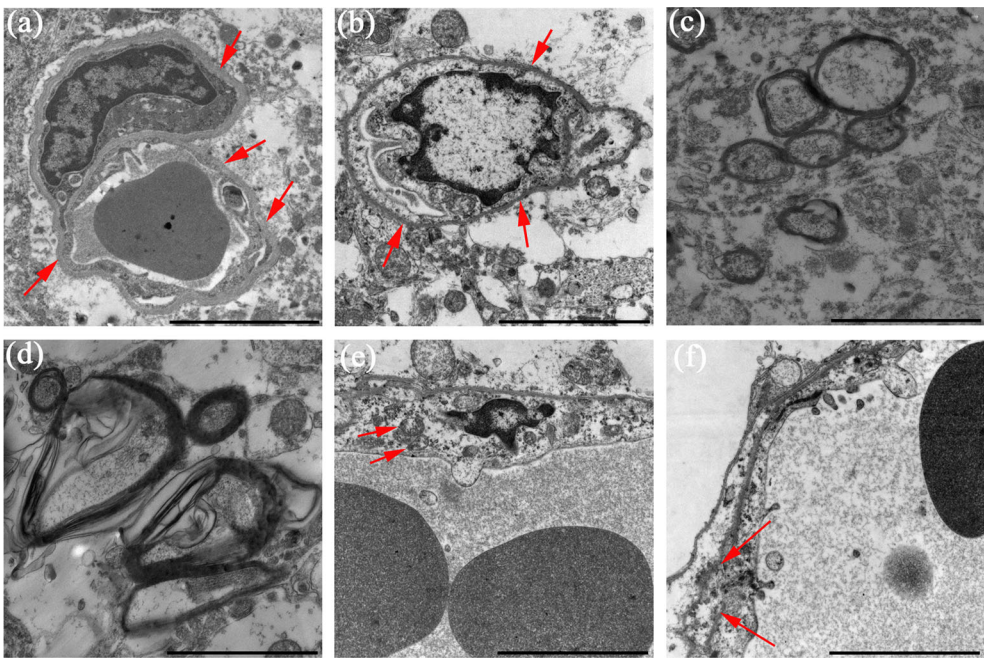

Fig. 7 Transmission electron microscopy of the brain samples from control and hydrocephalic animal. **a** Blood–brain barrier of the control animals. *Scale bar* 2 μm. **b** Blood–brain barrier of the experimental animals. *Scale bar* 2 μm. Thinning of the basal lamina is pointed by *red arrows*. **c** Microstructure of the white matter fibers in control animal. *Scale bar* 2 μm. **d** Ultrastructure alterations of the white matter fibers in the hydrocephalic animal. *Scale bar* 2 μm. **e** Swollen mitochondria in the endothelial cell is pointed with *red arrows*. *Scale bar* 2 μm **f** Disrupted basal lamina with glio-basal dissociation is shown (*red arrows*). *Scale bar* 2 μm

review by Hoza et al. [19] it was stated that one of the key biomarkers for clinical diagnosis of hydrocephalus progression could be DTI. In the study by Ivkovic et al. [21], it was shown that the implication of the parametric model for the shape of mean diffusivity histogram obtained from DTI can be of value in the differential diagnosis of normal pressure hydrocephalus from Alzheimer's disease and Parkinson's disease. Axial diffusivity of corona radiata was linearly correlated with ventricular size in patients with hydrocephalus [7]. If the shunting is applied, then as was demonstrated by Scheel et al. [36], there is an increase in FA values in patients with hydrocephalus. Another parameter ADC was also shown to have a clinical value. Thus, following CSF diversion in hydrocephalus patients there was an extensive decrease of ADC values [31].

The reported radiological changes had a good correlation with morphological data, indicating that MR characteristics (i.e., FA, ADC) could be reliably applied for the diagnosis and treatment efficacy assessment in patients with hydrocephalus.

Acknowledgments The authors are grateful to Olga G. Genbach, Nelly V. Koroleva, Dmitriy N. Suslov, Oleg V. Galibin, Tatiana V. Zakoldaeva, Irina V. Kononova, Yulia E. Shevchuk, Oleg A. Don for assistance in animal experiments.

Conflicts of interest None.

Funding This work was supported by grants from the Russian Foundation for Basic Research, nos. 140800614 and 130401299.

References

1. Bloch O, Auguste KI, Manley GT, Verkman AS (2006) Accelerated progression of kaolin-induced hydrocephalus in aquaporin-4-deficient mice. J Cereb Blood Flow Metab 26:1527–1537
2. Braun KP, de Graaf RA, Vandertop WP, Gooskens RH, Tulleken KA, Nicolay K (1998) In vivo 1H MR spectroscopic imaging and diffusion weighted MRI in experimental hydrocephalus. Magn Reson Med 40:832–839
3. Braun KP, Dijkhuizen RM, de Graaf RA, Nicolay K, Vandertop WP, Gooskens RH, Tulleken KA (1997) Cerebral ischemia and white matter edema in experimental hydrocephalus: a combined in vivo MRI and MRS study. Brain Res 757:295–298
4. Braun KP, van Eijsden P, Vandertop WP, de Graaf RA, Gooskens RH, Tulleken KA, Nikolay K (1999) Cerebral metabolism in experimental hydrocephalus: an in vivo 1H and 31P magnetic resonance spectroscopy study. J Neurosurg 91:660–668
5. Braun KP, Vandertop WP, Gooskens RH, Tulleken KA, Nicolay K (2000) NMR spectroscopic evaluation of cerebral metabolism in hydrocephalus: a review. Neurol Res 22:51–64
6. Castejón OJ (2009) Blood–brain barrier ultrastructural alterations in human congenital hydrocephalus and Arnold-Chiari malformation. Folia Neuropathol 47:11–19
7. Cauley KA, Cataltepe O (2014) Axial diffusivity of the corona radiata correlated with ventricular size in adult hydrocephalus. AJR Am J Roentgenol 203:170–179
8. Cherian S, Whitelaw A, Thoresen M, Love S (2004) The pathogenesis of neonatal post-hemorrhagic hydrocephalus. Brain Pathol 14: 305–311
9. Chua CO, Chahboune H, Braun A, Dummula K, Chua CE, Yu J, Ungvari Z, Sherbany AA, Hyder F, Ballabh P (2009) Consequences of intraventricular hemorrhage in a rabbit pup model. Stroke 40: 3369–3377
10. Collins P (1979) Experimental obstructive hydrocephalus in the rat: a scanning electron microscopic study. Neuropathol Appl Neurobiol 5: 457–468
11. De Lahunta A (1983) Veterinary neuroanatomy and clinical neurology, 2nd edn. WB Saunders, Philadelphia
12. Del Bigio MR, Kanfer JN, Zhang YW (1997) Myelination delay in the cerebral white matter of immature rats with kaolin-induced hydrocephalus is reversible. J Neuropathol Exp Neurol 56:1053–1066
13. Del Bigio MR, Khan OH, da Silva LL, Juliet PA (2012) Cerebral white matter oxidation and nitrosylation in young rodents with kaolin-induced hydrocephalus. J Neuropathol Exp Neurol 71:274–288
14. Del Bigio MR, Slobodian I, Schellenberg AE, Buist RJ, Kemp-Buors TL (2011) Magnetic resonance imaging indicators of blood–brain barrier and brain water changes in young rats with kaolin-induced hydrocephalus. Fluids Barriers CNS 8:22
15. Edvinsson L, West KA (1971) The time-course of intracranial hypertension as recorded in conscious rabbits after treatment with different amounts of intracisternally injected kaolin. Acta Neurol Scand 47: 439–450
16. Eskandari R, Abdullah O, Mason C, Lloyd KE, Oeschle AN, McAllister JP 2nd (2014) Differential vulnerability of white matter structures to experimental infantile hydrocephalus detected by diffusion tensor imaging. Childs Nerv Syst 30:1651–1661
17. Fishman RA (1992) Cerebrospinal fluid in diseases of the nervous system. W.B. Saunders, Philadelphia
18. Haworth CS, Sobieski MW, Scheld WM, Park TS (1990) *Staphylococcus aureus ventriculitis* treated with single-dose intraventricular vancomycin or daptomycin (LY146032): bacterial and antibiotic kinetics in hydrocephalic rabbits. Antimicrob Agents Chemother 34:245–251
19. Hoza D, Vlasák A, Hořínek D, Sameš M, Alfieri A (2014) DTI-MRI biomarkers in the search for normal pressure hydrocephalus aetiology: a review. Neurosurg Rev. doi:10.1007/s10143-014-0584-0
20. Ishii K, Hashimoto M, Hayashida K, Hashikawa K, Chang CC, Nakagawara J, Nakayama T, Mori S, Sakakibara R (2011) A multicenter brain perfusion SPECT study evaluating idiopathic normal-pressure hydrocephalus on neurological improvement. Dement Geriatr Cogn Disord 32:1–10
21. Ivkovic M, Liu B, Ahmed F, Moore D, Huang C, Raj A, Kovanlikaya I, Heier L, Relkin N (2013) Differential diagnosis of normal pressure hydrocephalus by MRI mean diffusivity histogram analysis. AJNR Am J Neuroradiol 34:1168–1174
22. Johnson MJ, Ayzman I, Wood AS, Tkach JA, Klauschie J, Skarupa DJ, McAllister JP, Luciano MG (1999) Development and characterization of an adult model of obstructive hydrocephalus. J Neurosci Methods 91:55–65
23. Johnston MG, Del Bigio MR, Drake JM, Armstrong D, Di Curzio DL, Bertrand J (2013) Pre- and post-shunting observations in adult sheep with kaolin-induced hydrocephalus. Fluids Barriers CNS 10: 24
24. Klarica M, Oresković D, Bozić B, Vukić M, Butković V, Bulat M (2009) New experimental model of acute aqueductal blockage in cats: effects on cerebrospinal fluid pressure and the size of brain ventricles. Neuroscience 158:1397–1405
25. Kobayashi S, Kato K, Rodríguez Guerrero A, Baba H, Yoshizawa H (2012) Experimental syringohydromyelia induced by adhesive arachnoiditis in the rabbit: changes in the blood-spinal cord barrier,

neuroinflammatory foci, and syrinx formation. J Neurotrauma 29: 1803–1816
26. Kondziella D, Eyjolfsson EM, Saether O, Sonnewald U, Risa O (2009) Gray matter metabolism in acute and chronic hydrocephalus. Neuroscience 159:570–577
27. Kondziella D, Sonnewald U, Tullberg M, Wikkelso C (2008) Brain metabolism in adult chronic hydrocephalus. J Neurochem 106:1515–1524
28. Kulkarni AV, Riva-Cambrin J, Browd SR, Drake JM, Holubkov R, Kestle JR, Limbrick DD, Rozzelle CJ, Simon TD, Tamber MS, Wellons JC 3rd, Whitehead WE, Hydrocephalus Clinical Research Network (2014) Endoscopic third ventriculostomy and choroid plexus cauterization in infants with hydrocephalus: a retrospective Hydrocephalus Clinical Research Network study. J Neurosurg Pediatr 14:224–229
29. Kulkarni AV, Riva-Cambrin J, Butler J, Browd SR, Drake JM, Holubkov R, Kestle JR, Limbrick DD, Simon TD, Tamber MS, Wellons JC 3rd, Whitehead WE, Hydrocephalus Clinical Research Network (2013) Outcomes of CSF shunting in children: comparison of Hydrocephalus Clinical Research Network cohort with historical controls: clinical article. J Neurosurg Pediatr 12:334–338
30. Kurt G, Cemil B, Borcek AO, Borcek P, Akyurek N, Sepici A, Ceviker N (2010) Infliximab administration reduces neuronal apoptosis on the optic pathways in a rabbit hydrocephalus model: a preliminary report. Br J Neurosurg 24:275–279
31. Leliefeld PH, Gooskens RH, Braun KP, Ramos LM, Uiterwaal CS, Regli LP, Tulleken CA, Kappelle LJ, Hanlo PW (2009) Longitudinal diffusion-weighted imaging in infants with hydrocephalus: decrease in tissue water diffusion after cerebrospinal fluid diversion. J Neurosurg Pediatr 4:56–63
32. Leliefeld PH, Gooskens RH, Vincken KL, Ramos LM, van der Grond J, Tulleken CA, Kappelle LJ, Hanlo PW (2008) Magnetic resonance imaging for quantitative flow measurement in infants with hydrocephalus: a prospective study. J Neurosurg Pediatr 2:163–170
33. Lu Y, Qian L, Zhang Q, Chen B, Gui L, Huang D, Cheng G, Chen L (2013) Palmitateinduces apoptosis in mouse aortic endothelial cells and endothelial dysfunction in mice fed high-calorie and high-cholesterol diets. Life Sci 92:1165–1173
34. Massicotte EM, Buist R, Del Bigio MR (2000) Altered diffusion and perfusion in hydrocephalic rat brain: a magnetic resonance imaging analysis. J Neurosurg 92:442–447
35. Reddy GK, Bollam P, Caldito G (2014) Long-term outcomes of ventriculoperitoneal shunt surgery in patients with hydrocephalus. World Neurosurg 81:404–410
36. Scheel M, Diekhoff T, Sprung C, Hoffmann KT (2012) Diffusion tensor imaging in hydrocephalus—findings before and after shunt surgery. Acta Neurochir (Wien) 154:1699–1706
37. Slobodian I, Krassioukov-Enns D, Del Bigio MR (2007) Protein and synthetic polymer injection for induction of obstructive hydrocephalus in rats. Cerebrospinal Fluid Res 4:9
38. Tarnaris A, Toma AK, Pullen E, Chapman MD, Petzold A, Cipolotti L, Kitchen ND, Keir G, Lemieux L, Watkins LD (2011) Cognitive, biochemical, and imaging profile of patients suffering from idiopathic normal pressure hydrocephalus. Alzheimers Dement 7:501–508
39. Torvik A, Stenwig AE, Finseth I (1981) The pathology of experimental obstructive hydrocephalus. A scanning electron microscopic study. Acta Neuropathol 54:143–147
40. Tully HM, Dobyns WB (2014) Infantile hydrocephalus: a review of epidemiology, classification and causes. Eur J Med Genet 57:359–368
41. Ueno M, Tomita S, Nakagawa T, Ueki M, Iwanaga Y, Ono J, Onodera M, Huang CL, Kanenishi K, Shimada A, Maekawa N, Sakamoto H (2006) Effects of aging and HIF-1alpha deficiency on permeability of hippocampal vessels. Microsc Res Tech 69:29–35
42. Vullo T, Manzo R, Gomez DG, Deck MD, Cahill PT (1998) A canine model of acute hydrocephalus with MR correlation. AJNR Am J Neuroradiol 19:1123–1125
43. Weller RO, Mitchell J, Griffin RL, Gardner MJ (1978) The effects of hydrocephalus upon the developing brain. Histological and quantitative studies of the ependyma and subependyma in hydrocephalic rats. J Neurol Sci 36:383–402
44. Wen YD, Wang H, Kho SH, Rinkiko S, Sheng X, Shen HM, Zhu YZ (2013) Hydrogen sulfide protects HUVECs against hydrogen peroxide induced mitochondrial dysfunction and oxidative stress. PLoS One 8:e53147
45. Yuan W, McAllister JP 2nd, Lindquist DM, Gill N, Holland SK, Henkel D, Rajagopal A, Mangano FT (2012) Diffusion tensor imaging of white matter injury in a rat model of infantile hydrocephalus. Childs Nerv Syst 28:47–54
46. Ziegelitz D, Starck G, Kristiansen D, Jakobsson M, Hultenmo M, Mikkelsen IK, Hellström P, Tullberg M, Wikkelsø C (2014) Cerebral perfusion measured by dynamic susceptibility contrast MRI is reduced in patients with idiopathic normal pressure hydrocephalus. J Magn Reson Imaging 39:1533–1542

Comment

This is a well-written and illustrated study investigating the correlation between the changes of neuroradiological and morphological parameters in an experimental model of acute obstructive hydrocephalus. It is clear that conventional MRI sequences provide accurate data to help the diagnosis of acute and chronic hydrocephalus. Nonetheless, the use of diffusion sequences demonstrated that values of apparent diffusion coefficient (ADC) in the periventricular and periaqueductal areas were significantly increased and fractional anisotropy was decreased in the zones of periventricular, periaqueductal white matter and corpus callosum. These features could be attributed to the integrity loss of the blood–brain barrier. Histological analysis confirms this hypothesis and results presented here by the authors are in accordance with previously published observations of ultrastructural changes in blood–brain barrier in patients with congenital hydrocephalus. Together, the results of this study suggest that restoration of blood–brain barrier permeability may play a role in some stage of the treatment of hydrocephalus. Further studies are warranted.

Alfredo Conti
Messina, Italy